energies

MDPI

Article

Numerical and Experimental Performance Evaluation of a Photovoltaic Thermal Integrated Membrane Desalination System

Sajid Ali *, Fahad Al-Amri and Farooq Saeed

Mechanical and Energy Engineering Department, Imam Abdulrahman Bin Faisal University, Dammam 31441, Saudi Arabia

* Correspondence: sakzada@iau.edu.sa

Abstract: Membrane desalination (MD) is preferred over other desalination techniques since it requires a lower temperature gradient. Its performance can be further enhanced by preheating the intake of saline water. In this context, a novel solar-assisted air gap membrane desalination (AGMD) system was hypothesized. The motivation was derived from the fact that the use of solar energy to provide power and a pre-heating source for the intake of saline water can offer a sustainable alternative that can further enhance the acceptance of MD systems. Since solar panels suffer from a loss of efficiency as they heat up during operation, a solar-assisted air gap membrane desalination (AGMD) system can help to improve the overall system performance by (1) providing the necessary pumping power to operate the system and (2) improving solar panel performance by exchanging heat using water that is (3) used to pre-heat the saline water necessary for increased performance of the AGMD system. To verify the hypothesis, a solar-assisted AGMD system for freshwater production was theoretically designed, fabricated locally, and then tested experimentally. The effect of the process operating parameters and the ambient conditions on the overall performance of the proposed solar-assisted AGMD desalination unit is presented in detail, both theoretically and experimentally. The results indicated a direct correlation between the permeate flux, saline hot feed temperature, and hot feed flow rate. In addition, an inverse relationship between the cold feed temperature, cold feed flow rate, and the air gap thickness of the module was also observed and reported, thus, validating the hypothesis that a solar-assisted air gap membrane desalination (AGMD) system can help to boost performance.

Keywords: membrane desalination; renewable energy; solar-assisted desalination; permeate flux; air gap membrane desalination

Citation: Ali, S.; Al-Amri, F.; Saeed, F. Numerical and Experimental Performance Evaluation of a Photovoltaic Thermal Integrated Membrane Desalination System. *Energies* **2022**, *15*, 7417. https://doi.org/10.3390/en15197417

Academic Editors: Sharul Sham Dol and Anang Hudaya Muhamad Amin

Received: 9 March 2022
Accepted: 21 April 2022
Published: 10 October 2022

1. Introduction

The continuing increase in the global human population has led to a continuous decline in access to fresh water [1]. The problem is further compounded by climate change due to the uneven redistribution of freshwater resources around the globe [2]. Well over a billion people around the world do not have access to safe drinking water [3]. It is estimated that by 2025, more than 2.8 billion people worldwide will face water shortages [4]. The urgency of increasing access to fresh water and providing alternatives is a major concern for humanity, in general, and the scientific community. Distillation has the potential to address this concern and it has been acknowledged and duly recognized as a practical approach to overcoming the problem of freshwater scarcity [5,6]. Distillation techniques employing various methods, such as reverse osmosis, multi-effects, multistage flashes, and membranes, are some of the possible ways to desalinate seawater [7,8].

In various regions of the world, large-scale reverse osmosis (RO) has been used to provide drinkable water from seawater [9]. The reverse osmosis and multistage flash techniques share the credit for producing the highest volume of fresh water in the world

(43.5%) [10,11]. Reverse osmosis, which is a pressure-driven membrane separation process, is highly effective for desalinating seawater along the coastal areas, such as those around the Arabian peninsula [12]. Although this method has a lower maintenance cost, the installation and operating cost, along with susceptibility to fouling, which is an undesirable phenomenon, make this process unsuitable for small-scale desalination [13–15]. In the search for distillation techniques that are independent of conventional fuel resources, membrane distillation (MD) stands out since it has the ability to directly utilize solar thermal energy [16,17]. Membrane distillation relies on the difference in temperature between both sides of the hydrophobic membrane. The membrane used in this process prevents the liquid phase from being present but allows for the transfer of the vapor phase [18,19]. The temperature difference between both sides of the membrane results in a vapor pressure difference, which is the main driving force behind the transfer of vapors from the hot saline feed side of the membrane to the cold feed side [20]. The MD process has several distinguishable attributes, making it a better choice over other desalination techniques [21], such as lower resistance to mass transfer, lower operating hydrostatic pressure, and lower operating temperature [22,23]. In the MD process, low-grade thermal energy can be used as a heat source [24]. Four widely used MD configurations are (i) air gap membrane distillation (AGMD), (ii) vacuum membrane distillation (VMD), (iii) direct contact membrane distillation (DCMD), and (iv) sweep gas membrane distillation (SGMD) [25,26].

In comparison to these processes, AGMD has relatively low energy consumption. In addition, compared to DCMD and VMD, AGMD can operate at lower operating temperatures and lower operating hydrostatic pressures [27,28]. AGMD's ability to attain extremely high salt rejection factors adds to its appeal. Membrane fouling is also less of an issue than with AGMD as compared to other pressure-driven desalination techniques, such as RO. There is no need for substantial pre-treatment, which is required in the RO procedure [29]. Desalination necessitates a large amount of energy, which comes at a considerable expense. It is reported in [30] that the desalination technique necessitates a 9-to-22-fold increase in energy expenditure over typical surface water treatment methods. Huyen et al. [31] provided a thorough overview of the energy requirements of different desalination processes. The comparison is made in terms of total equivalent electric consumption (kWh/m^3), which is the sum of electric and thermal energy usage (kWh/m^3). Multi-stage flash (MSF), thermal-vapor compression (TVC), electrodialysis (ED), multi-effect distillation (MED), and reverse osmosis (RO) have electrical energy consumption needs of 5 kWh/m^3, 1.8 kWh/m^3, 3.2 kWh/m^3, 2.2 kWh/m^3, and 7 kWh/m^3, respectively [32,33].

In AGMD, a condensing surface is placed between the membrane and the cold flow channel. Compared to other MD configurations, the presence of the air gap significantly reduces the conduction losses, thus increasing the thermal efficiency [34,35]. Additionally, the air gap layer allows for direct collection of the permeate [36]. An optimized AGMD model was developed for seawater desalination in [37]. An innovative AGMD module with improved efficiency was presented by Tian et al. [38]. The proposed AGMD design significantly improved productivity. The primary performance index was estimated using the regression model. The thermal efficiency of the AGMD module was evaluated for a particular flow rate in [39]. The effect of the material and type of membrane used in an AGMD module on its performance was experimentally studied in [40]. It was reported in [41] that a larger membrane pore size results in higher permeate flux. It was shown that replacing the flat condensing plate with a channeled plate improved the process efficiency by 50% [42]. For household applications in UAE, a novel AGMD system was designed and developed to co-produce hot and fresh water [43]. The efficiency of a solar panel is directly linked to its surface temperature. Usually, up to 80% of the solar radiation is transformed into heat [44]. It has been shown that for a single degree increase in temperature, the effectiveness of a PV solar cell is reduced by 0.45% [45]. The electrical efficiency of the solar panels requires constant cooling to extract the excessive heat from its surface [46]. Thus, in the proposed design, by extracting thermal energy from the panel, it will act as a passive

cooling agent to reduce the panel surface temperature. The proposed system was tested experimentally. Operation and control-related issues of an AGMD system were discussed by Change et al. [47,48].

A thorough review of the literature revealed that there have been only a limited number of studies on the performance analysis of solar-assisted AGMD desalination systems. In the quest for further improvements, the current paper presents a novel design of a solar-assisted AGMD desalination system for freshwater production. The salient feature of this new design is that the saline water is pre-heated as it is passed through a liquid container integrated at the back of a solar PV panel. It is postulated that the pre-heated saline water will result in improved performance of an AGMD desalination system. In this regard, the current paper presents the design of the proposed system along with a detailed theoretical thermodynamic and heat and mass transfer analysis accompanied by experiment observations and measurements to help validate the improved performance of the proposed system. The effect of various process operating parameters is also presented in detail.

In the sections that follow, the first details of the design of the proposed model, including the in-house designed and built AGMD module, are presented. Next, the theoretical model of the complete process is described, along with its numerical implementation. Then, the experimental setup is described, along with different instrumentations for different measurements. The numerical and experimental results are then used to present the effect of various process operating parameters on the AGMD system performance. Finally, the study ends with important conclusions and some recommendations for future work.

2. Model Development

As shown in Figure 1, the saline solution is heated by passing it through the hot water at the back of the solar panel. The main components of the experimental setup are the air gap membrane module, water chiller, and solar panel integrated with a passive water-cooling system. The rear of the panel is filled with water, as the surface temperature of the solar panel rises, the temperature of the water at the rear of the panel also increases. A pipe (main pipe) carrying the saline solution, supplied from a tank via a pump, is passed through the heated water and given as an input to the AGMD module through a connecting pipe, Figure 2. Desalinated water is collected in a container placed below the AGMD module.

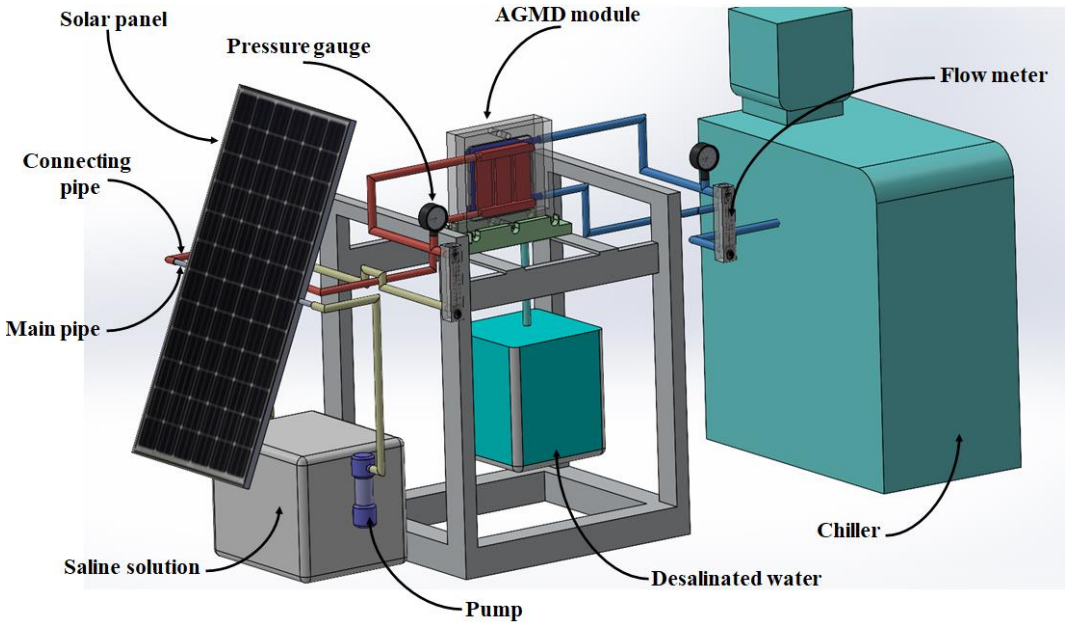

Figure 1. Proposed system.

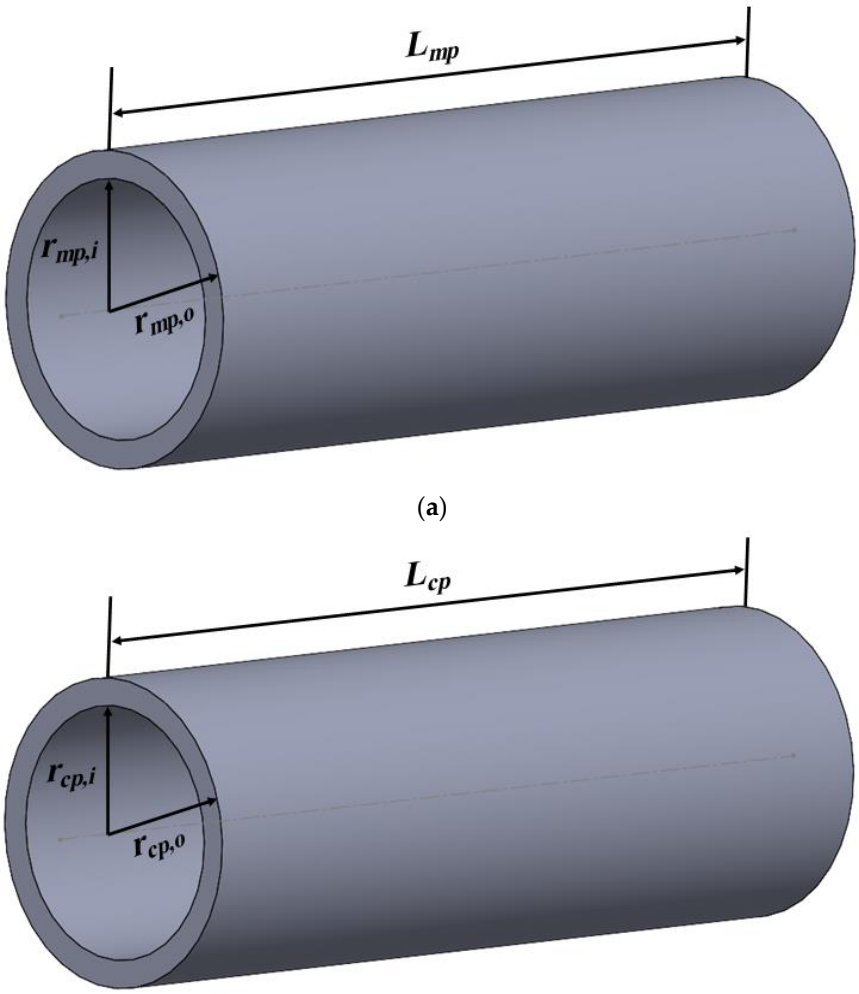

Figure 2. (**a**) Main pipe (mp) passing through the hot water and (**b**) connecting pipe (cp) that connects the main pipe with the AGMD module.

The temperature of the hot water surrounding the main pipe is "T_w" and temperature of the ambient air surrounding the connecting pipe is "T_a". The mean inlet temperatures for main and connecting pipes are "$T_{mp,mi}$" and "$T_{cp,mi}$", respectively. Similarly, the mean outlet temperatures for the main and connecting pipes are "$T_{mp,mo}$" and "$T_{cp,mo}$", respectively, Figure 3. The temperature differences for the main and connecting pipes are defined as

$$\Delta T_{mp,o} = T_w - T_{mp,mo} \quad (1)$$

$$\Delta T_{mp,i} = T_w - T_{mp,mi} \quad (2)$$

$$\Delta T_{cp,o} = T_w - T_{cp,mo} \quad (3)$$

$$\Delta T_{cp,i} = T_w - T_{cp,mi} \quad (4)$$

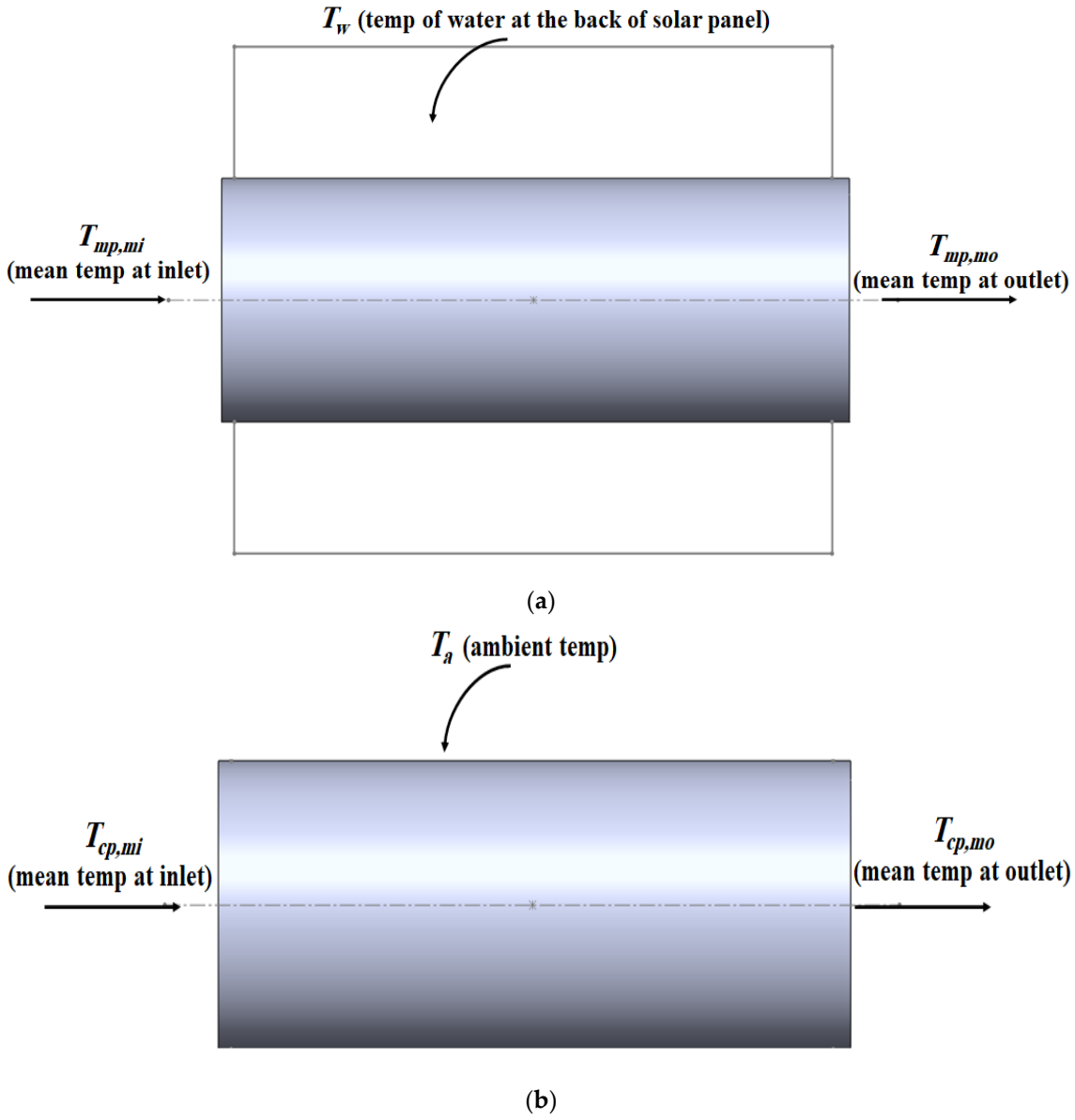

Figure 3. Inlet, outlet, and surrounding temperatures at the (**a**) main pipe (surrounded by hot water) and (**b**) connecting pipe (surrounded by ambient air).

The log-mean temperature differences for the main and connecting pipes are

$$\Delta T_{mp,lm} = \frac{\Delta T_{mp,o} - \Delta T_{mp,i}}{\ln\left(\frac{\Delta T_{mp,o}}{\Delta T_{mp,i}}\right)} \quad (5)$$

$$\Delta T_{cp,lm} = \frac{\Delta T_{cp,o} - \Delta T_{cp,i}}{\ln\left(\frac{\Delta T_{cp,o}}{\Delta T_{cp,i}}\right)} \quad (6)$$

The rates of heat transfer in the main and connecting pipes are given as

$$q_{mp} = \bar{U}_{mp} A_{mp,s} \Delta T_{mp,lm} \quad (7)$$

$$q_{cp} = \bar{U}_{cp} A_{cp,s} \Delta T_{cp,lm} \quad (8)$$

since we can write

$$\bar{U}_{mp}A_{mp,s} = \frac{1}{R_{mp}} \tag{9}$$

$$\bar{U}_{cp}A_{cp,s} = \frac{1}{R_{cp}} \tag{10}$$

where the corresponding thermal resistances are

$$R_{mp} = \frac{1}{h_{mp,1}2\pi r_{mp,i}L_{mp}} + \frac{\ln\left(\frac{r_{mp,o}}{r_{mp,i}}\right)}{2\pi k_{mp}L_{mp}} + \frac{1}{h_{mp,2}2\pi r_{mp,o}L_{mp}} \tag{11}$$

$$R_{cp} = \frac{1}{h_{cp,1}2\pi r_{cp,i}L_{cp}} + \frac{\ln\left(\frac{r_{cp,o}}{r_{cp,i}}\right)}{2\pi k_{cp}L_{cp}} + \frac{1}{h_{cp,2}2\pi r_{cp,o}L_{cp}} \tag{12}$$

The surface heat transfer coefficients for the main pipe in the above equations can be found from the associated Nusselt number correlations:

$$h_{mp,1} = \frac{K_{mp}}{D_{mp,i}}\overline{Nu}_{mp,1}$$

$$h_{mp,2} = \frac{K_{mp}}{D_{mp,0}}\overline{Nu}_{mp,2}$$

Here,

$$\overline{Nu}_{mp,1} = 0.023Re_{mp}{}^{\frac{4}{5}}Pr^{n}$$

$$\overline{Nu}_{mp,2} = 0.36$$

Similarly, for the connecting pipes, the associated heat transfer coefficients and corresponding Nusselt number correlations are

$$h_{cp,1} = \frac{K_{cp}}{D_{cp,i}}\overline{Nu}_{cp,1}$$

$$h_{cp,2} = \frac{K_{cp}}{D_{cp,0}}\overline{Nu}_{cp,2}$$

$$\overline{Nu}_{cp,1} = 0.023Re_{cp}{}^{\frac{4}{5}}Pr^{n}$$

$$\overline{Nu}_{cp,2} = 0.40$$

The rates of heat transfer in the main and connecting pipes in terms of the flow rates and heat capacities are

$$q_{mp} = \dot{m}C_P\left(T_{mp,mi} - T_{mp,mo}\right) \tag{13}$$

$$q_{cp} = \dot{m}C_P\left(T_{cp,mi} - T_{cp,mo}\right) \tag{14}$$

Substituting Equations (5) and (6) into Equations (7) and (8) and equating the resultant with Equations (13) and (14), respectively, and then rearranging the resulting equations gives

$$T_{mp,mo} = T_w - \left(T_w - T_{mp,mi}\right)\exp\left(\frac{-\bar{U}_{mp}A_{mp,s}}{\dot{m}C_P}\right) \tag{15}$$

$$T_{cp,mo} = T_a - (T_a - T_{cp,mi}) \exp\left(\frac{-\bar{U}_{cp} A_{cp,s}}{\dot{m} C_P}\right) \quad (16)$$

Thus, for given main and connecting pipe mean inlet temperatures, pipe geometry, and flow rates, the Nusselt number correlations were used to determine the surface heat transfer coefficients and the thermal resistance. Then, the overall heat transfer coefficients (U) were determined, and finally, the mean outlet temperatures were calculated. Since the fluid properties were evaluated at an initial guess temperature, an iterative procedure was adopted to ensure that the fluid properties corresponded to the film temperature based on the mean inlet and converged outlet temperatures.

Different sections of the proposed AGMD module are shown in Figure 4, which are the (i) hot flow chamber, (ii) membrane layer, (iii) air gap, (iv) cooling plate, and (v) cold flow chamber.

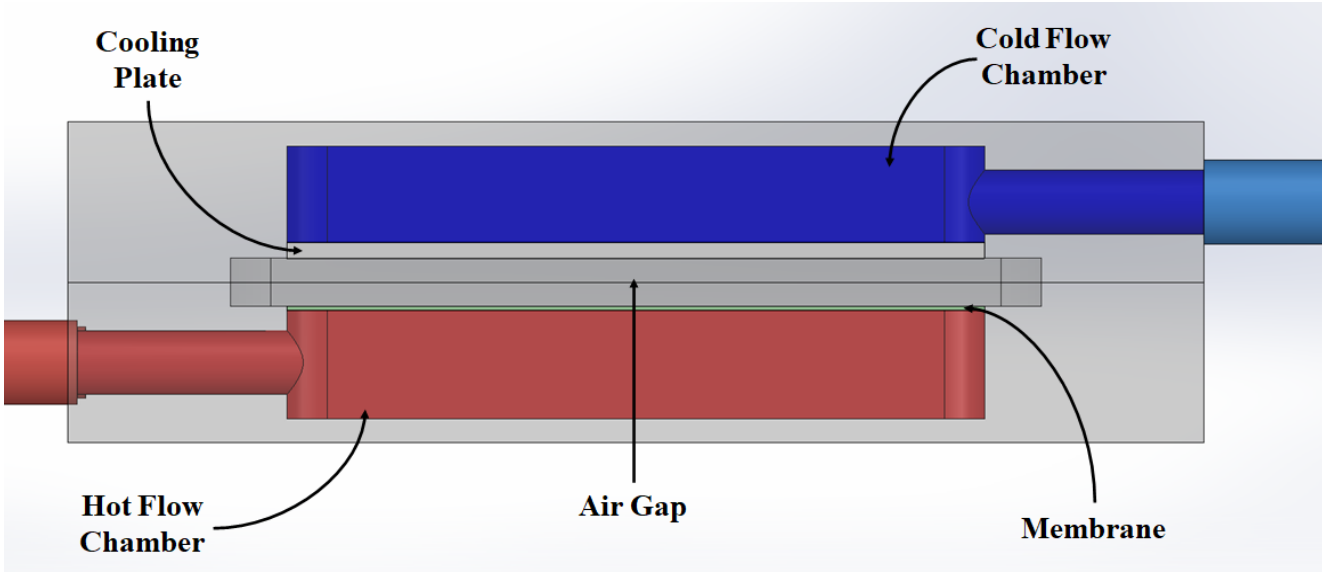

Figure 4. Proposed AGMD module.

The mass transferred along the material of the membrane relies on the difference in vapor pressure between the membrane sides. The correlation is described between mass transferred (J_{wvp}) and vapor pressure difference (ΔP) along the membrane and it can be written as follows [49]:

$$J_{wvp} = M_c(P_{hm} - P_{cm}) \quad (17)$$

where Mc is the mass transfer coefficient, P_{hm} is the vapor pressure on the feeding side of the membrane, and P_{cm} is the vapor pressure on the condensing side of the membrane. Substituting the overall mass transfer coefficient (Mc) into Equation (17), a simplified equation of the water vapor permeate flux is given as

$$J_{wvp} = \frac{\varepsilon P_{total} D_{water-air}}{RT_m \frac{(P_{afm} - P_{acm})}{\ln\left(\frac{P_{afm}}{P_{acm}}\right)}} (P_{hm} - P_{cm}) \quad (18)$$

where $D_{water-air}$ is the diffusion of the mass in the water vapor and the air, ε is the membrane porosity, and Tm is the mean temperature. Antoine equations [49] are applied to obtain the values of P_{hm} and P_{cm}. In the case of salt dissolved in the hot fluid, Raoult's law

is used to express the vapor pressure, where P_{hm} is replaced with P_{hhm} to include the salt concentrate effect in the hot feed as follows:

$$P_{hhm} = (1 - CM_{NaCl})P_{hm} \tag{19}$$

where

$$CM_{NaCl} = \frac{\text{NaCl concentration } \left(\frac{g}{L}\right)}{58.44 \left(\frac{g}{mol}\right)} \tag{20}$$

Heat transfer analysis over the membrane is performed to calculate T_{hm} and T_{cm}. Through the hot saline solution, the heat transferred is presented as

$$Q_h = \left(h_h + J_{wvp}C_f\right)\left(T_{cp,mo} - T_{hm}\right) \tag{21}$$

where h_h is the heat transfer coefficient at the hot feed side, C_f is the coefficient of specific heat, and T_{hm} is the temperature at the hot side of the membrane.

Applying the methodology adopted in [49], the heat transfer from the membrane to the cold solution passing through the air gap and cooling plate is given as (i) heat transferred from the hot side of the membrane to the condensation liquid interface Q_1, (ii) heat transferred via convection through the condensate layer Q_2, (iii) heat transfer via conduction into the cooling plate Q_3, and (iv) heat transferred via convection between the coolant solution and the cold plate Q_4, which are expressed as

$$Q_1 = h_1\left(T_{hm} - T_{cp}\right) + J_{wvp}Q_{vp} \tag{22}$$

$$Q_2 = h_2\left(T_{cp} - T_p\right) \tag{23}$$

$$Q_3 = k_c\left(T_p - T_{cc}\right) \tag{24}$$

$$Q_4 = h_3\left(T_{cc} - T_c\right) \tag{25}$$

Here, h_i is the coefficient of heat transfer, T_{cp} is the temperature of the condensate side of the cooling plate, T_p is the temperature of the cooling plate, T_{cc} is the temperature of the cold fluid side of the plate, T_c is the temperature of the cold fluid, k_c is the thermal conductivity per unit thickness of the plate, and Q_{vp} is the enthalpy of vaporization. The overall heat moved from the condensate layer to the cold solution can be written as

$$Q_c = h_T\left(T_{cp} - T_c\right) \tag{26}$$

where h_T is the heat transfer coefficient from membrane to the cold solution and is given as

$$h_T = \left(\frac{1}{h_2} + \frac{1}{k_c} + \frac{1}{h_3}\right)^{-1} \tag{27}$$

Therefore, the temperature of the hot side of the membrane and cold side of the cooling plate is obtained in the following form:

$$T_{hm} = T_{cp,mo} - \frac{H_T}{h_h}\left(\left(T_{cp,mo} - T_c\right) + \frac{J_{wvp}Q_{vp}}{h_1}\right) \tag{28}$$

and

$$T_{cp} = T_c + \frac{H_T}{h_h}\left(\left(T_{cp,mo} - T_c\right) + \frac{J_{wvp}Q_{vp}}{h_1}\right) \tag{29}$$

with

$$H_T = \left(\frac{1}{h_h} + \frac{1}{h_1} + \frac{1}{h_T}\right)^{-1} \tag{30}$$

The solution of Equation (18), along with Equations (28) and (29), will yield the permeate flux through the membrane under given setup conditions.

3. Experimental Setup

The designed and developed experimental setup used in the study is shown in Figure 5. The key components of the experimental setup were the (i) air gap membrane module, (ii) water chiller, and (iii) solar PV panel integrated with a passive water-cooling system.

Figure 5. Experimental setup.

A commercial-scale PV panel with a 330 W peak output and size of 1990 × 995 × 35 mm, as shown in Figure 5, was used in the experimental setup. The rear of the PV panel was enclosed in a tin sheet to form a closed container to hold the water (57 L) such that the water was in direct contact with the backside of the solar panel to absorb the heat from the solar panel. As the surface temperature of the solar panel rose, it heated the water at the back of the panel.

A pipe carrying the saline solution was passed through the heated water. The temperature of the saline solution increased as a result of heat transfer between water at the back of the panel and the pipe. The AGMD unit was manufactured from acrylic with the dimensions of 100 mm × 100 mm to accommodate a membrane with dimensions of 60 mm × 60 mm to desalinate the saline water with a high enough availability of resources. Each chamber was machined from the inside to allow for a thickness of 15 mm for water. A Thermo Scientific Arctic A40/AC200 (Chiller) with a built-in pump (Figure 6a) was used to pump the cold water through the coolant chamber of the AGMD module through the condensation plate that was located between the air gap and the coolant channel, and the coolant water went back to the chiller. The inlet of the AGMD module was connected to the pipe's exit containing the saline solution and passed through the back of the solar panel. The AGMD module consisted of two identical flow chambers, namely, hot and cold flow. A membrane was placed adjacent to the hot flow chamber. At the same time, an aluminum plate (condensation surface) was placed adjacent to the cold flow chamber. Rubber spacers were used within the module components to create the air gap. The pressure difference between the sections was the main driving force causing a permeate flux to flow from the

hot solution to the condensation section. Other components of the setup included (i) two flow meters (Omega FL 50000; Figure 6b) to measure and control the flow of hot saline solution and cold-water solution, (ii) two Baumer pressure gauges (Figure 6c) at the inlet of the cold and hot flow chambers, and (iii) thermocouples to measure temperatures at both sides of the AGMD module.

(**a**) (**b**) (**c**)

Figure 6. (**a**) Chiller with a built-in pump, (**b**) flow meters (Omega FL 50,000), and (**c**) Baumer pressure gauges.

As per the product's technical specification, k-type thermocouples have a precision of ±2.5 percent. The calibration of these inserted thermocouples was further tested by utilizing a standard calibration process for more accurate results. These thermocouples provide a linear relationship across a wide temperature range of up to 250 °C. The permeate flux was measured using a beaker (10 cm diameter) with a calibrated scale with an accuracy of ±1 mm. This translated into a measurement accuracy of the permeate flux to within ±0.785 kg/m^2/h. For the flow measurement, the Omega FL 50000A was used, and for pressure measurement, the Baumer pressure gauge was used, with the accuracies of ±5% and ±1.6%, respectively. The FL 50000A has a robust, one-piece acrylic shell, metal associated components, panel-mountable backside suction, and discharge ports with high accuracy.

4. Results and Discussions

The results of the numerical and experimental investigations of the process parameters are presented in this section. One of the critical process parameters was the temperature of the hot feed, which depends on the PV panel surface temperature and the ambient temperature. The ambient temperature and solar panel surface temperature were recorded, as shown in Figures 7 and 8.

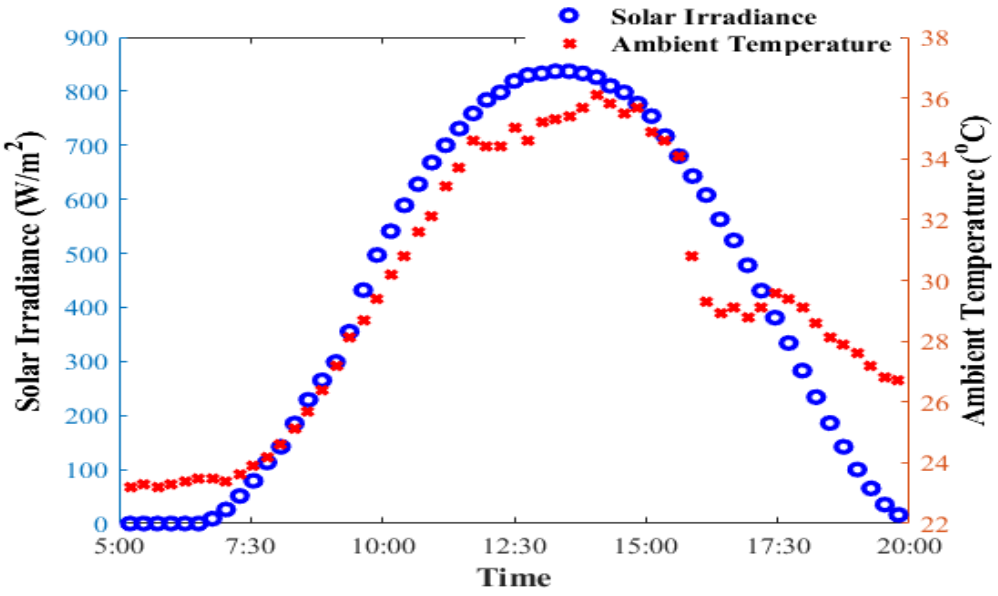

Figure 7. Measured solar irradiance and ambient temperature.

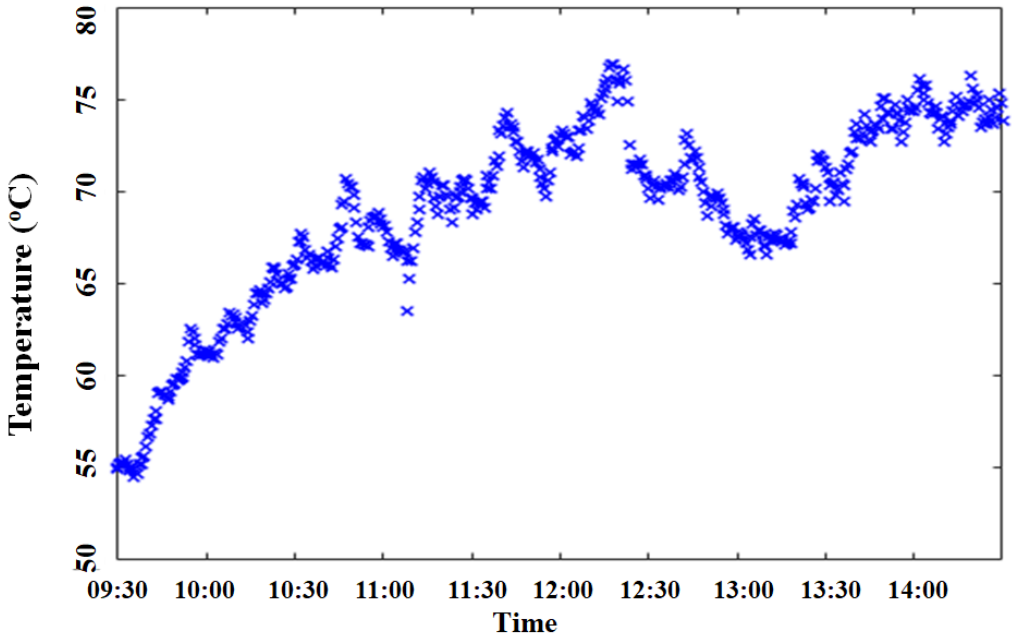

Figure 8. The surface temperature of the solar panel.

The hourly global solar radiation and ambient temperature on 12 April 2021, in the city of Dammam are shown in Figure 7. The ambient temperature was observed to remain above 30 °C during the period of 10 am to 3 pm. The measured surface temperature of the solar panel crossed the 75 °C mark during the same period (Figure 8).

The mean temperatures of the hot saline at the outlet of the main and connecting pipes are shown in Figure 9. The temperature of the water (Tw) at the back of the solar panel surrounding the main pipe was 70 °C. To account for the heat losses from the connecting pipe, the ambient temperature (Ta) in the numerical solution was kept at 35 °C. The effect of the heat losses from the connecting pipe was quite obvious in terms of the time taken to reach the steady temperature.

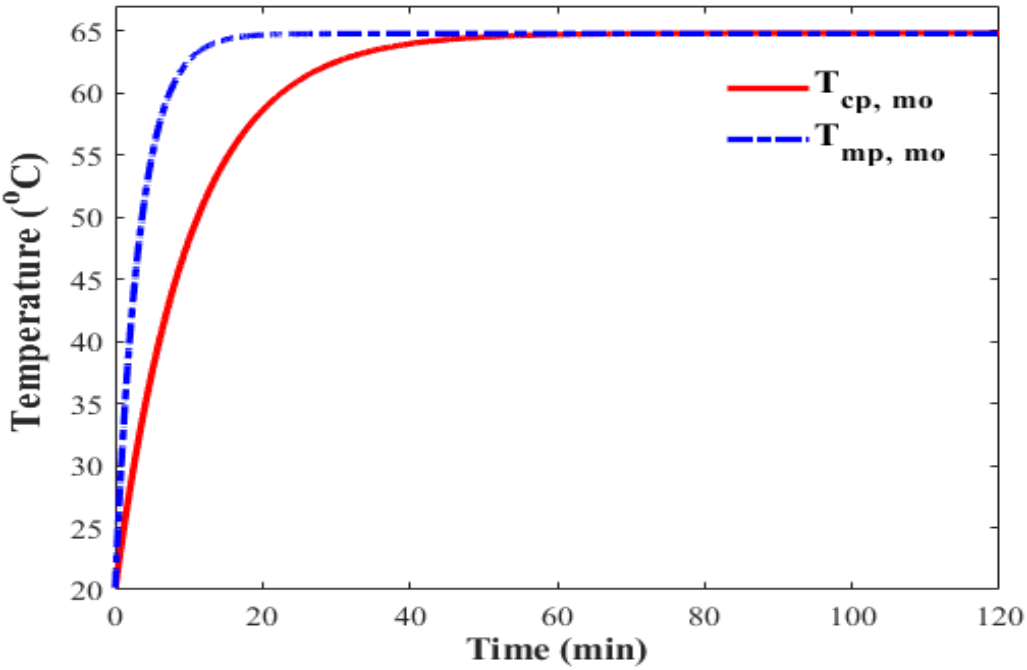

Figure 9. Mean outlet temperatures of the main pipe ($T_{mp,mo}$) and connecting pipe ($T_{cp,mo}$).

The effects of the feed rate of the hot saline (through the hot flow chamber) and cold fluid (through the cold flow chamber) on the permeate are shown in Figures 10 and 11.

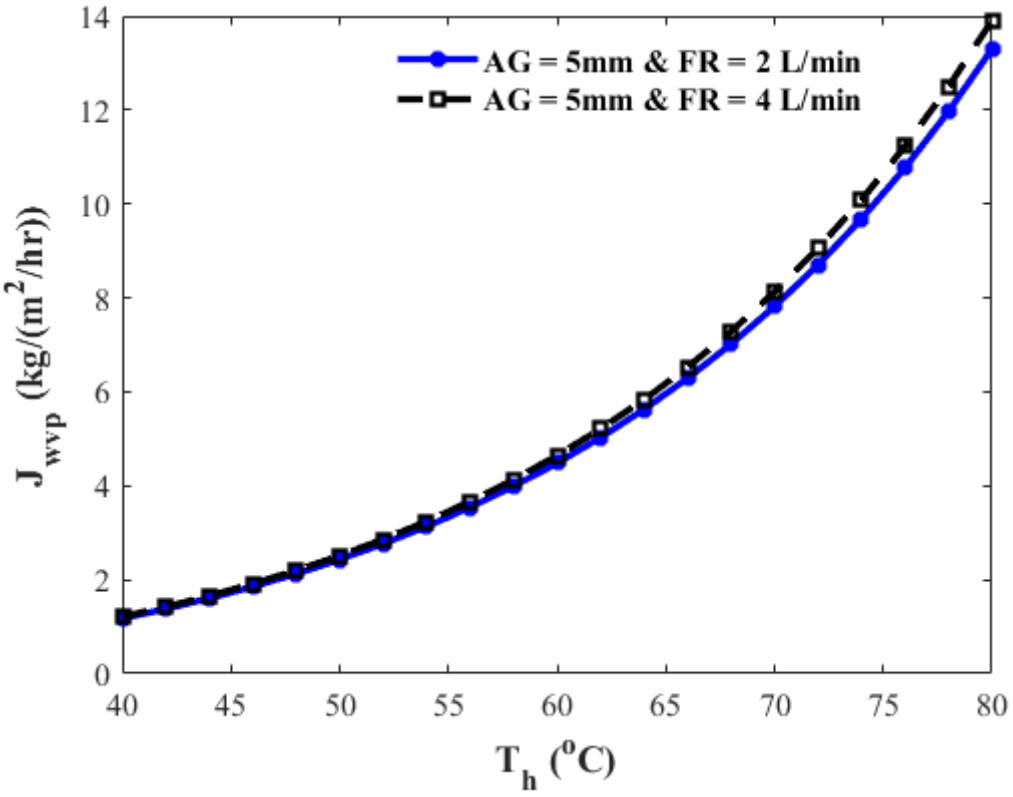

Figure 10. Effect of the hot feed (FR = 2 and 4 L/min) on the permeate (J_{wvp}) at different hot feed temperatures (T_h) (air gap thickness (AG) of 5 mm).

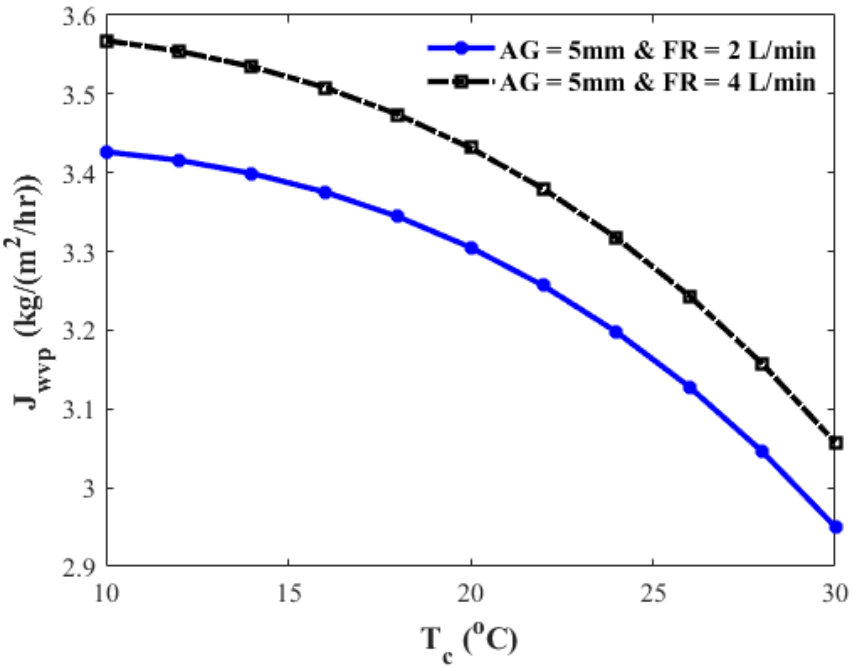

Figure 11. Effect of the hot feed (FR = 2 and 4 L/min) on the J_{wvp} at different cold feed temperatures (T_c) (air gap thickness (AG) of 5 mm).

The effect of the hot feed temperature on the Jwvp at a constant cold feed temperature (20 °C) and fixed air gap thickness (5 mm) is presented in Figure 10. It is evident that when the hot feed temperature increased, the permeate increased. Increasing the feed of the hot solution from 2 L/min to 4 L/min produce a slim increase in the permeate corresponding to the hot feed temperature above 60 °C. Similarly, the effect of the cold feed temperature on the permeate at a constant hot feed temperature (55 °C) and fixed air gap thickness (5 mm) is presented in Figure 11. As expected, when the cold feed temperature increased, the permeate decreased. A visible rise in the permeate was obtained by boosting the hot feed rate from 2 L/min to 4 L/min.

The effect of the cold feed on the permeate flux is presented in Figures 12 and 13.

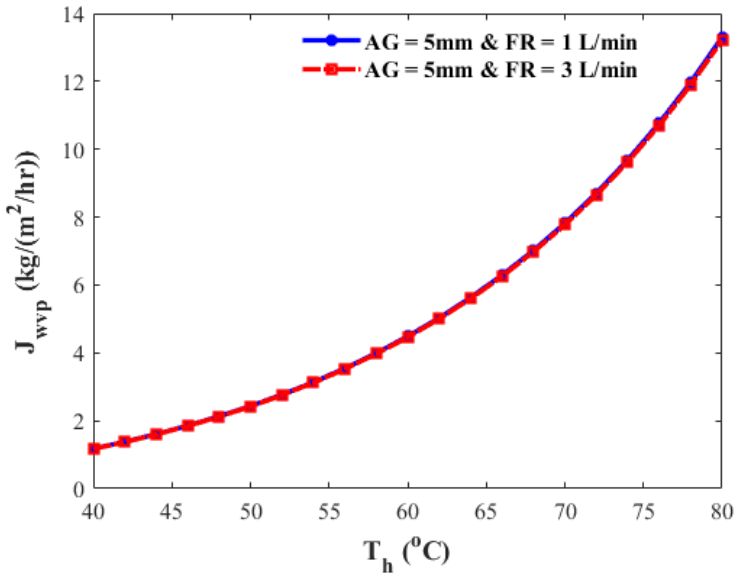

Figure 12. Effect of the cold feed (FR = 1 and 3 L/min) on the J_{wvp} at different hot feed temperatures (T_h) (air gap thickness (AG) of 5 mm).

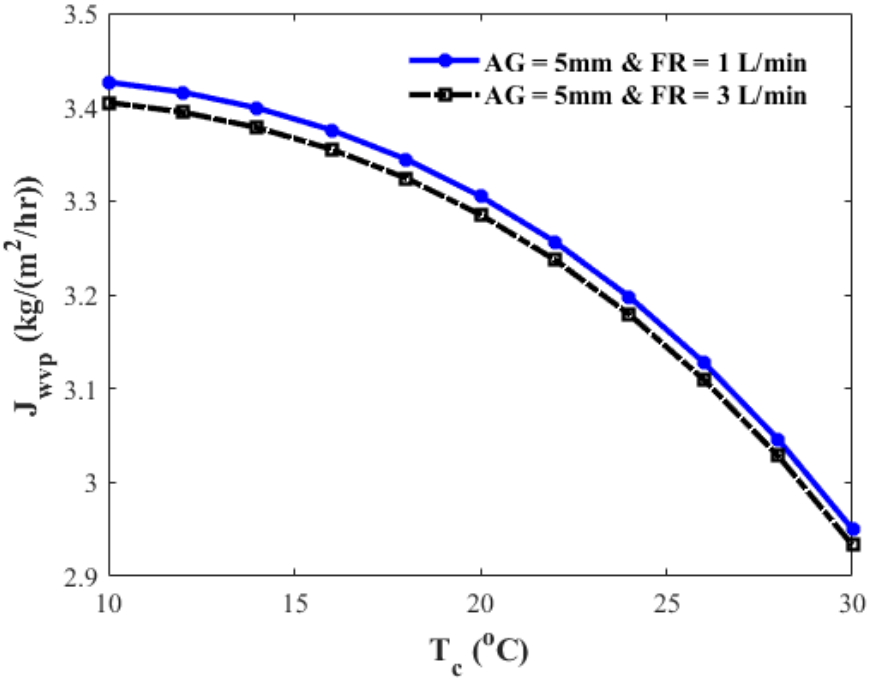

Figure 13. Effect of the cold feed (FR = 1 and 3 L/min) on the J_{wvp} at different cold feed temperatures (T_c) (air gap thickness (AG) of 5 mm).

While keeping the cold feed at a constant temperature (20 °C), the permeate corresponding to the cold feed of 1 L/min and 3 L/min at varying hot feed temperatures remained unchanged, as shown in Figure 12. In contrast, when keeping the hot feed temperature constant (55 °C), a drop in the flux was observed with the increase in the cold feed from 1 L/min to 3 L/min at different cold feed temperatures (Figure 13).

The effect of the air gap thickness (AG) on the permeate is presented in Figures 14 and 15.

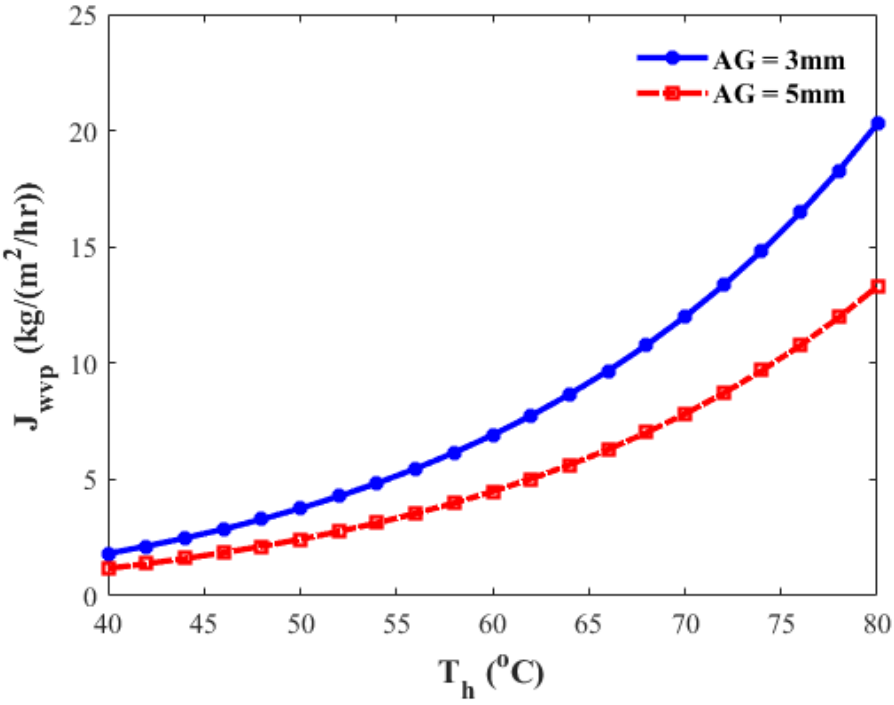

Figure 14. Effect of the air gap thickness (AG = 3 and 5 mm) on the J_{wvp} at different hot feed temperatures (T_h) (hot feed of 2 L/min and cold feed of 1 L/min).

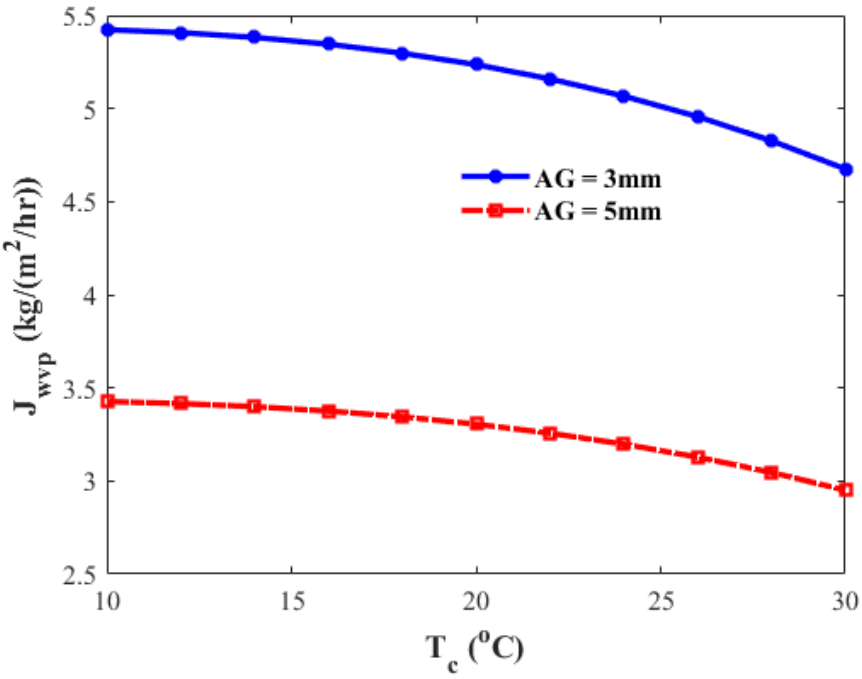

Figure 15. Effect of the air gap thickness (AG = 3 and 5 mm) on the J_{wvp} at different cold feed temperatures (T_c) (hot feed of 2 L/min and cold feed of 1 L/min).

The effect of the air gap thickness on the permeate is shown in Figure 14 at different hot feed temperatures. Increasing the air gap thickness had an adverse impact on the permeate, as it tended to decrease when the air gap thickness was raised from 3 mm to 5 mm. A similar effect, i.e., higher air gap thickness corresponded to lower permeate flux, was also observed in the case of varying cold feed temperature (Figure 15).

An analysis of the airgap membrane desalination parameters was also undertaken experimentally. The permeate flux was measured under different operating conditions. The effects of hot and cold temperatures on the permeate at a constant cold feed temperature (20 °C) are presented in Figures 16 and 17.

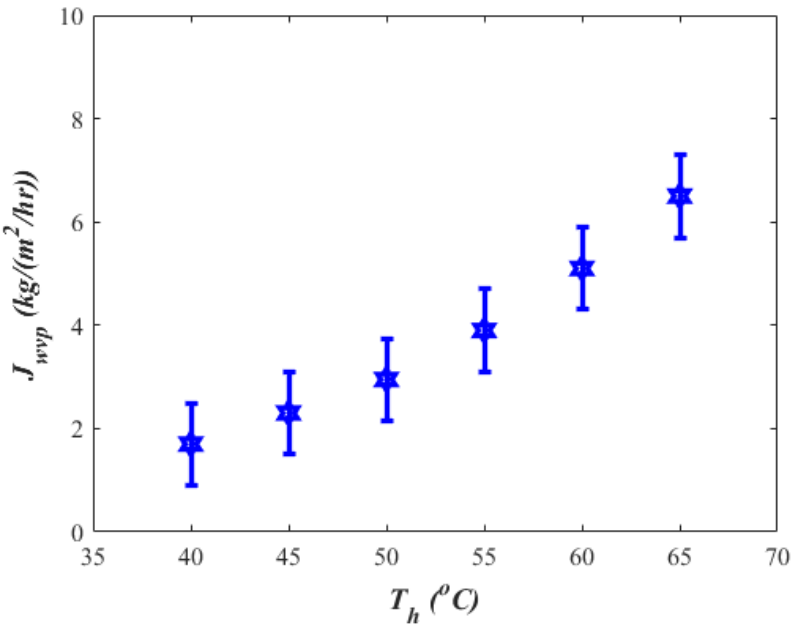

Figure 16. J_{wvp} at different hot feed temperatures (T_h).

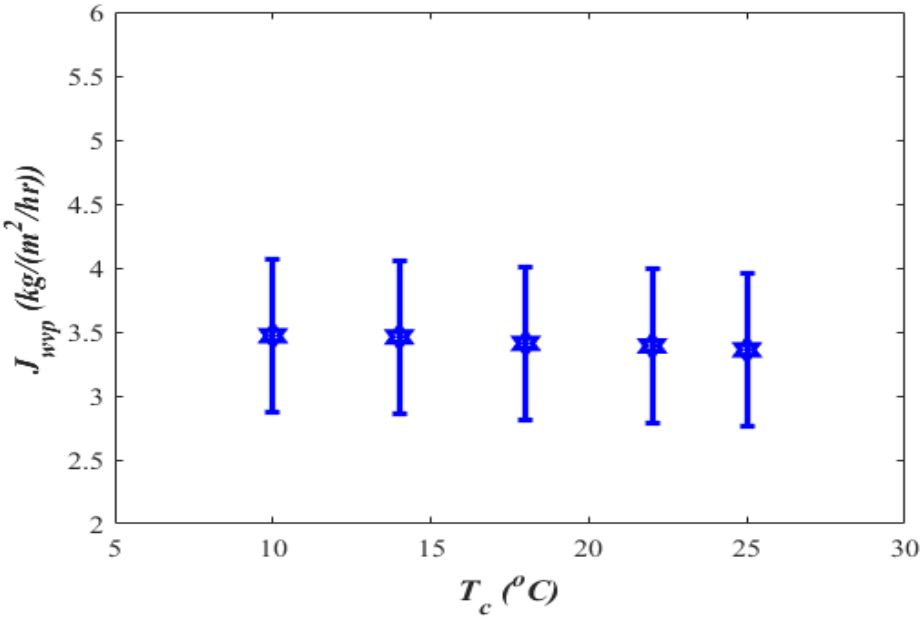

Figure 17. J_{wvp} at different cold feed temperatures (T_c).

The hot feed was kept at 4 L/min, while the cold feed was kept at 1 L/min. The experimental results were found to be in accord with the numerical results presented in the earlier section. Increasing the hot feed temperature resulted in an increase in the permeate (Figure 16) and increasing the cold feed temperature resulted in a decrease in the permeate (Figure 17). The permeate fluxes obtained from the experimental tests (EV) were compared with those obtained from the numerical simulations (NV) (Figure 18).

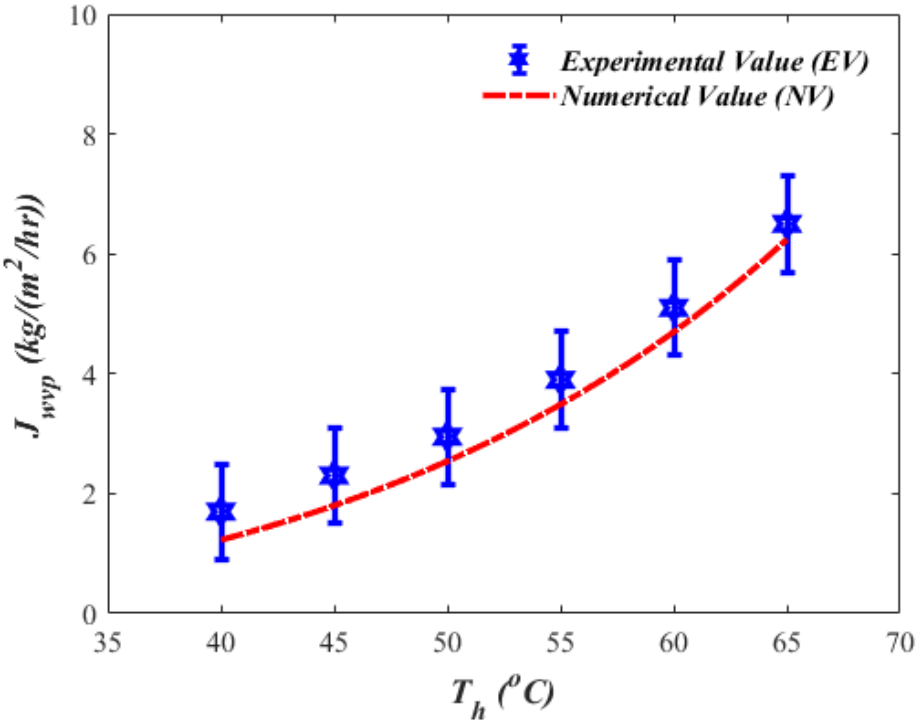

Figure 18. Permeate flux (J_{wvp}) comparison, experimental vs. numerical.

It is evident from the caparison that the experimental results (EV) and numerical values were quite comparable. The numerical results were well within the expected accuracy range (±0.785 kg/m^2/h) of the experimental setup.

Figure 19 shows the energy consumption comparison as a result of photovoltaic thermal integration. The results showed that a 39% saving in energy consumption was afforded by the use of a photovoltaic thermal integrated membrane desalination system since the system provided electrical power to run the pump and the chiller, in addition to providing the thermal energy to heat the saline water, thus eliminating the use of a heater.

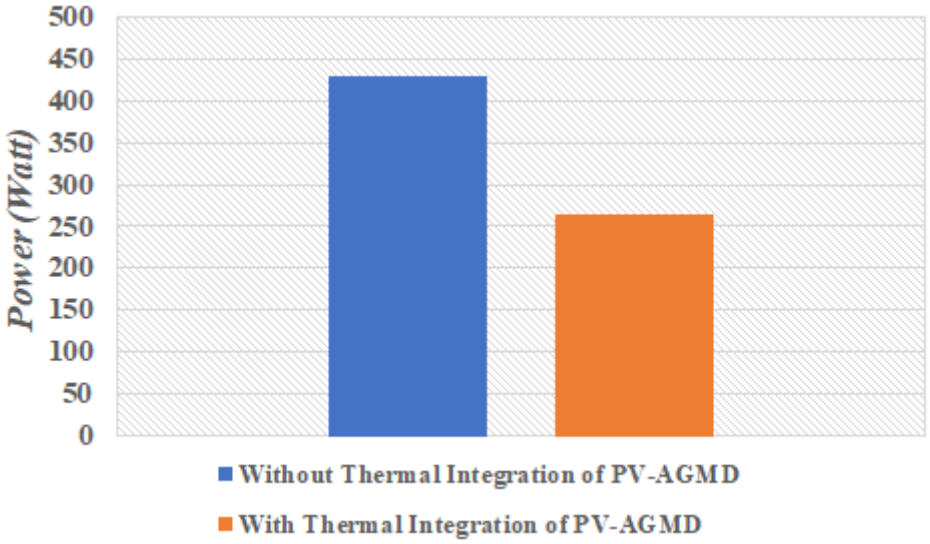

Figure 19. Energy consumption comparison.

5. Conclusions

A novel solar-assisted AGMD system was proposed that utilized solar energy as a heating source for the intake saline solution. A prototype of the proposed design was built and experimentally tested to validate the concept and the numerical model. Detailed thermodynamic, heat, and mass transfer analyses are presented. In the analysis, the temperature of water at the back of the solar panel that surrounded the main pipe was observed to reach above 70 °C. To account for the heat losses from the connecting pipe, the ambient temperature in the numerical solution was kept at 35 °C. The effect of the heat losses from the connecting pipe was noted in terms of the time taken to reach the steady temperature. It was observed that increasing the hot feed temperature on the permeate flux at a constant cold feed temperature (20 °C) and fixed air gap thickness (5 mm) increased the permeate flux. In addition, increasing the feed rate of hot solution from 2 L/min to 4 L/min resulted in a slight rise in the permeate flux corresponding to the hot feed temperature above 60 °C. In contrast, by increasing the cold feed temperature on the permeate flux at a constant hot feed temperature (55 °C) and fixed air gap thickness (5 mm), the permeate flux tended to decrease. Furthermore, it was observed that keeping a constant cold feed temperature (20 °C) at different cold feed flow rates did not have an effect on the permeate flux. On the other hand, when keeping the hot feed temperature constant (55 °C), a decrease in the permeate flux was observed with an increase in the cold feed rate from 1 L/min to 3 L/min at different cold feed temperatures. Increasing the air gap thickness resulted in a decrease in the permeate flux. The permeate fluxes obtained from the experimental tests were compared with those obtained from the numerical simulations. It was observed from the caparison that the experimental results and numerical values were quite comparable. The numerical results were well within the expected accuracy range (±0.785 kg/m^2/h) of the experimental setup.

Author Contributions: Data curation, S.A.; Investigation, S.A., F.A.-A. and F.S.; Methodology, S.A., F.A.-A. and F.S.; Project administration, F.A.-A.; Resources, F.A.-A.; Software, S.A.; Supervision, F.A.-A.; Visualization, S.A.; Writing—original draft, S.A.; Writing—review and editing, F.A.-A. and F.S. All authors have read and agreed to the published version of the manuscript.

Funding: This research was funded by the Deputyship for Research & Innovation, Ministry of Education in Saudi Arabia grant project number IF-2020-024-Eng.

Institutional Review Board Statement: Not applicable.

Informed Consent Statement: Not applicable.

Data Availability Statement: The data that support the findings of this study are available on request from the corresponding author. The data are not publicly available due to privacy or ethical restrictions.

Acknowledgments: The authors extend their appreciation to the Deputyship for Research and Innovation, Ministry of Education in Saudi Arabia, for funding this research work through the project number IF-2020-024-Eng at Imam Abdulrahman bin Faisal University/College of Engineering.

Conflicts of Interest: The authors declare no conflict of interest.

List of Symbols

$A_{mp,s}$	Main pipe surface area
C_P	Specific heat capacity
$D_{cp,o}$	Outer diameter of connecting pipe
$D_{mp,o}$	Outer diameter of main pipe
J_{wvp}	Mass transferred
k_{mp}	Thermal conductivity of main pipe
L_{mp}	Length of main pipe
$\dot{m}$	Mass flow rate
P_{hm}	Vapor pressure on the feeding side
q_{cp}	Rate of heat transfer (connecting pipe)
R_{cp}	Thermal resistance of connecting pipe
$r_{cp,i}$	Inner radius of connecting pipe
$r_{mp,o}$	Outer radius of main pipe
T_a	Ambient air temperature
$T_{cp,mo}$	Mean outlet temperature (connecting pipe)
$T_{mp,mo}$	Mean outlet temperature (main pipe)
$\bar{U}_{cp}$	Overall heat transfer coefficient for connecting pipe
$\Delta T_{mp,lm}$	Log-mean temperature differences
$A_{cp,s}$	Connecting pipe surface area
$D_{cp,i}$	Inner diameter of connecting pipe
$D_{mp,i}$	Inner diameter of main pipe
h_T	Overall convection heat transfer coefficient
k_{cp}	Thermal conductivity of connecting pipe
L_{cp}	Length of connecting pipe
Mc	Mass transfer coefficient
P_{cm}	Vapor pressure on the condensing side
Q_{vp}	Enthalpy of vaporization
q_{mp}	Rate of heat transfer (main pipe)
R_{mp}	Thermal resistance of main pipe
$r_{cp,o}$	Outer radius of connecting pipe
$r_{mp,i}$	Inner radius of main pipe
$T_{cp,mi}$	Mean inlet temperature (connecting pipe)
$T_{mp,mi}$	Mean inlet temperature (main pipe)
T_w	Water temperature at the back of panel
$\bar{U}_{mp}$	Overall heat transfer coefficient for main pipe
ΔP	Vapor pressure difference

References

1. Pangarkar, B.L.; Sane, M.G.; Guddad, M. Reverse osmosis and membrane distillation for desalination of groundwater: A review. *Int. Sch. Res. Not.* **2011**, *2011*, 523124. [CrossRef]
2. Chen, Y.H.; Hung, H.G.; Ho, C.D.; Chang, H. Economic design of solar-driven membrane distillation systems for desalination. *Membranes* **2021**, *11*, 15. [CrossRef] [PubMed]
3. Shannon, M.A.; Bohn, P.W.; Elimelech, M.; Georgiadis, J.G.; Marinas, B.J.; Mayes, A.M. Science and technology for water purification in the coming decades. *Nature* **2008**, *452*, 301–310. [CrossRef] [PubMed]
4. Hameeteman, E. *Future Water (In)Security: Facts, Figures, and Predictions*; Global Water Institute: Columbus, OH, USA, 2013; pp. 1–16.
5. Elimelech, M.; Phillip, W.A. The future of seawater desalination: Energy, technology, and the environment. *Science* **2011**, *333*, 712–717. [CrossRef] [PubMed]
6. Duong, H.C.; Cooper, P.; Nelemans, B.; Cath, T.Y.; Nghiem, L.D. Evaluating energy consumption of air gap membrane distillation for seawater desalination at pilot scale level. *Sep. Purif. Technol.* **2016**, *166*, 55–62. [CrossRef]
7. Marni Sandid, A.; Bassyouni, M.; Nehari, D.; Elhenawy, Y. Experimental and simulation study of multichannel air gap membrane distillation process with two types of solar collectors. *Energy Convers. Manag.* **2021**, *243*, 114431. [CrossRef]
8. Shim, W.G.; He, K.; Gray, S.; Moon, I.S. Solar energy assisted direct contact membrane distillation (DCMD) process for seawater desalination. *Sep. Purif. Technol.* **2015**, *143*, 94–104. [CrossRef]
9. World Health Organization. *Safe Drinking-Water from Desalination*; World Health Organization: Geneva, Switzerland, 2011.
10. Al-Subaie, K.Z. Precise way to select a desalination technology. *Desalination* **2007**, *206*, 29–35. [CrossRef]
11. Al-Salmi, M.; Laqbaqbi, M.; Al-Obaidani, S.; Al-Maamari, R.S.; Khayet, M.; Al-Abri, M. Application of membrane distillation for the treatment of oil field produced water. *Desalination* **2020**, *494*, 114678. [CrossRef]
12. Qin, J.-J.; Lay, W.C.L.; Kekre, K.A. Recent developments and future challenges of forward osmosis for desalination: A review. *Desalin. Water Treat.* **2012**, *39*, 123–136. [CrossRef]
13. Petersen, R.J. Composite reverse osmosis and nanofiltration membranes. *J. Memb. Sci.* **1993**, *83*, 81–150. [CrossRef]
14. Mouiya, M.; Abourriche, A.; Bouazizi, A.; Benhammou, A.; El Hafiane, Y.; Abouliatim, Y.; Nibou, L.; Oumam, M.; Ouammou, M.; Smith, A. Flat ceramic microfiltration membrane based on natural clay and Moroccan phosphate for desalination and industrial wastewater treatment. *Desalination* **2018**, *427*, 42–50. [CrossRef]
15. Krzeminski, P.; Gil, J.A.; van Nieuwenhuijzen, A.F.; van der Graaf, J.H.J.M.; van Lier, J.B. Flat sheet or hollow fibre—comparison of full-scale membrane bio-reactor configurations. *Desalin. Water Treat.* **2012**, *42*, 100–106. [CrossRef]
16. Wang, P.; Chung, T.-S. Recent advances in membrane distillation processes: Membrane development, configuration design and application exploring. *J. Memb. Sci.* **2015**, *474*, 39–56. [CrossRef]
17. Chafidz, A.; Al-Zahrani, S.; Al-Otaibi, M.N.; Hoong, C.F.; Lai, T.F.; Prabu, M. Portable and integrated solar-driven desalination system using membrane distillation for arid remote areas in Saudi Arabia. *Desalination* **2014**, *345*, 36–49. [CrossRef]
18. Drioli, E.; Ali, A.; Macedonio, F. Membrane distillation: Recent developments and perspectives. *Desalination* **2015**, *356*, 56–84. [CrossRef]
19. Alkhudhiri, A.; Darwish, N.; Hilal, N. Membrane distillation: A comprehensive review. *Desalination* **2012**, *287*, 2–18. [CrossRef]
20. Rabie, M.; Elkady, M.F.; El-Shazly, A.H. Effect of channel height on the overall performance of direct contact membrane distillation. *Appl. Therm. Eng.* **2021**, *196*, 117262. [CrossRef]
21. Lawson, K.W.; Lloyd, D.R. Membrane distillation. *J. Memb. Sci.* **1997**, *124*, 1–25. [CrossRef]
22. Al-Obaidani, S.; Curcio, E.; Macedonio, F.; Di Profio, G.; Al-Hinai, H.; Drioli, E. Potential of membrane distillation in seawater desalination: Thermal efficiency, sensitivity study and cost estimation. *J. Memb. Sci.* **2008**, *323*, 85–98. [CrossRef]
23. Cheng, L.-H.; Lin, Y.-H.; Chen, J. Enhanced air gap membrane desalination by novel finned tubular membrane modules. *J. Memb. Sci.* **2011**, *378*, 398–406. [CrossRef]
24. Cath, T.Y.; Adams, V.D.; Childress, A.E. Experimental study of desalination using direct contact membrane distillation: A new approach to flux enhancement. *J. Memb. Sci.* **2004**, *228*, 5–16. [CrossRef]
25. Miao, Q.; Zhang, Y.; Cong, S.; Guo, F. Experimental investigation on floating solar-driven membrane distillation desalination modules. *Membranes* **2021**, *11*, 304. [CrossRef] [PubMed]
26. Attia, H.; Osman, M.S.; Johnson, D.J.; Wright, C.; Hilal, N. Modelling of air gap membrane distillation and its application in heavy metals removal. *Desalination* **2017**, *424*, 27–36. [CrossRef]
27. Gude, V.G.; Nirmalakhandan, N.; Deng, S. Renewable and sustainable approaches for desalination. *Renew. Sustain. Energy Rev.* **2010**, *14*, 2641–2654. [CrossRef]
28. Jönsson, A.-S.; Wimmerstedt, R.; Harrysson, A.-C. Membrane distillation-a theoretical study of evaporation through microporous membranes. *Desalination* **1985**, *56*, 237–249. [CrossRef]
29. Alklaibi, A.M.; Lior, N. Transport analysis of air-gap membrane distillation. *J. Memb. Sci.* **2005**, *255*, 239–253. [CrossRef]
30. Voutchkov, N. Energy use for membrane seawater desalination–current status and trends. *Desalination* **2018**, *431*, 2–14. [CrossRef]
31. Do Thi, H.T.; Pasztor, T.; Fozer, D.; Manenti, F.; Toth, A.J. Comparison of desalination technologies using renewable energy sources with life cycle, pestle, and multi-criteria decision analyses. *Water* **2021**, *13*, 3023. [CrossRef]
32. Al Washahi, M.; Gopinath, A.S. Techno Economical Feasibility Analysis of Solar Powered RO Desalination in Sultanate of Oman. In Proceedings of the 2017 9th IEEE-GCC Conference and Exhibition (GCCCE), Manama, Bahrain, 8–11 May 2017; pp. 1–9.

33. Cherif, H.; Belhadj, J. Environmental life cycle analysis of water desalination processes. In *Sustainable Desalination Handbook*; Elsevier: Amsterdam, The Netherlands, 2018; pp. 527–559.
34. Alquraish, M.M.; Mejbri, S.; Abuhasel, K.A.; Zhani, K. Experimental investigation of a pilot solar-assisted permeate gap membrane distillation. *Membranes* **2021**, *11*, 336. [CrossRef]
35. Duong, H.C.; Chivas, A.R.; Nelemans, B.; Duke, M.; Gray, S.; Cath, T.Y.; Nghiem, L.D. Treatment of RO brine from CSG produced water by spiral-wound air gap membrane distillation—A pilot study. *Desalination* **2015**, *366*, 121–129. [CrossRef]
36. Guillén-Burrieza, E.; Zaragoza, G.; Miralles-Cuevas, S.; Blanco, J. Experimental evaluation of two pilot-scale membrane distillation modules used for solar desalination. *J. Memb. Sci.* **2012**, *409–410*, 264–275. [CrossRef]
37. Guillén-Burrieza, E.; Blanco, J.; Zaragoza, G.; Alarcón, D.-C.; Palenzuela, P.; Ibarra, M.; Gernjak, W. Experimental analysis of an air gap membrane distillation solar desalination pilot system. *J. Memb. Sci.* **2011**, *379*, 386–396. [CrossRef]
38. Tian, R.; Gao, H.; Yang, X.H.; Yan, S.Y.; Li, S. A new enhancement technique on air gap membrane distillation. *Desalination* **2014**, *332*, 52–59. [CrossRef]
39. Elhenawy, Y.; Elminshawy, N.A.S.; Bassyouni, M.; Alanezi, A.A.; Drioli, E. Experimental and theoretical investigation of a new air gap membrane distillation module with a corrugated feed channel. *J. Memb. Sci.* **2020**, *594*, 117461. [CrossRef]
40. Singh, D.; Sirkar, K.K. Desalination by air gap membrane distillation using a two hollow-fiber-set membrane module. *J. Memb. Sci.* **2012**, *421*, 172–179. [CrossRef]
41. Geng, H.; Wu, H.; Li, P.; He, Q. Study on a new air-gap membrane distillation module for desalination. *Desalination* **2014**, *334*, 29–38. [CrossRef]
42. Bahar, R.; Hawlader, M.N.A.; Ariff, T.F. Channeled coolant plate: A new method to enhance freshwater production from an air gap membrane distillation (AGMD) desalination unit. *Desalination* **2015**, *359*, 71–81. [CrossRef]
43. Kumar, N.T.U.; Martin, A.R. Co-production performance evaluation of a novel solar combi system for simultaneous pure water and hot water supply in urban households of UAE. *Energies* **2017**, *10*, 481. [CrossRef]
44. Siddiqui, M.U.; Ali, S.; Khan, S.; Ali, S.; Horoub, M.M. Optimum Tilt Angles of Solar Collectors in Saudi Arabia. In Proceedings of the 3rd International Conference on Electrical, Communication, and Computer Engineering, Kuala Lumpur, Malaysia, 12–13 June 2021; pp. 12–13. [CrossRef]
45. Wu, S.-Y.; Guo, F.-H.; Xiao, L. A review on the methodology for calculating heat and exergy losses of a conventional solar PV/T system. *Int. J. Green Energy* **2015**, *12*, 379–397. [CrossRef]
46. Al-Amri, F.; Maatallah, T.S.; Al-Amri, O.F.; Ali, S.; Ali, S.; Ateeq, I.S.; Zachariah, R.; Kayed, T.S. Innovative technique for achieving uniform temperatures across solar panels using heat pipes and liquid immersion cooling in the harsh climate in the Kingdom of Saudi Arabia. *Alex. Eng. J.* **2022**, *61*, 1413–1424. [CrossRef]
47. Chang, H.; Liau, J.-S.; Ho, C.-D.; Wang, W.-H. Simulation of membrane distillation modules for desalination by developing user's model on Aspen Plus platform. *Desalination* **2009**, *249*, 380–387. [CrossRef]
48. Chang, H.; Wang, G.-B.; Chen, Y.-H.; Li, C.-C.; Chang, C.-L. Modeling and optimization of a solar driven membrane distillation desalination system. *Renew. Energy* **2010**, *35*, 2714–2722. [CrossRef]
49. Guijt, C.M.; Meindersma, G.W.; Reith, T.; De Haan, A.B. Air gap membrane distillation: 1. Modelling and mass transport properties for hollow fibre membranes. *Sep. Purif. Technol.* **2005**, *43*, 233–244. [CrossRef]